scientific reports

Check for updates

OPEN

Seismic characterization of inland and coastal sabkhas using V_P, V_S, seismic anisotropy, and attenuation

Ahmed Eleslambouly[1]✉, Mohammed Y. Ali[1], Fateh Bouchaala[1], Ammar El-Husseiny[2], Abdullatif Al-Shuhail[2], Sherif M. Hanafy[2] & Jun Matsushima[3]

Sabkhas represent abundant topographic environments along the Arabian Gulf and are increasingly relevant to hydrocarbon exploration and urban development. Their complex geological and hydrogeological settings significantly control near-surface seismic properties, influencing seismic velocity contrasts, attenuation ($Q_P{}^{-1}$), and anisotropy. This study presents the first integrated application of P-wave velocity (V_P), S-wave velocity (V_S), V_P/V_S ratio, seismic anisotropy, and $Q_P{}^{-1}$ attenuation analysis in sabkha environments, applied to the mature coastal sabkha of Abu Dhabi (CSAD) and the immature inland sabkha of Jayb Uwayyid (SJUW). Seismic refraction and multichannel analysis of surface waves (MASW) were used to obtain V_P and V_S, compute the V_P/V_S ratio, and estimate seismic anisotropy and attenuation. Three distinctive zones were delineated in both sabkhas using the produced tomograms. The shallowest dry zone with V_P<428 m/s, V_S <261 m/s and ratios of 1-2 with a thickness of 1-5 m, respectively, a transition partially saturated zone with V_P<1900 m/s, V_S <760 m/s and ratios of 1.5-2.5 extend up to 8 m in CSAD and 6 m in SJUW, a fully saturated zone, extending below the partially saturated zone, is defined by higher velocities (V_P >1900 m/s, V_S>760 m/s) and ratios increasing toward ~2–4.5 with depth. $Q_P{}^{-1}$ values reach up to 0.05 in both sabkhas, aligning with the hydrological zones, indicating fluid-related attenuation driven by seawater-brine interactions at CSAD and artesian upwelling at SJUW from continental brines. The uppermost parts of CSAD elevated velocities reflect a lithified hardground layer, while its elevated anisotropy marks its complex sedimentary and hydrological evolution. These results highlight the complexity of mature CSAD associated with elevated stratigraphy and hydrological conditions that affect the seismic signal.

Keywords Sabkha, Multichannel analysis of surface waves (MASW), Seismic waves, V_P/V_S, Seismic attenuation, Anisotropy, Near-surface geophysics

Sabkha is an Arabic term commonly used to describe salt-encrusted flats covering sand, silt, or clay beds[1]. These soils are typically loose and underlain by hypersaline groundwater at shallow depth (< 1 m)[2]. They predominantly consist of quartz, with main cementing minerals varying between aragonite, gypsum, anhydrite, and halite, or a combination, and mineral concentrations vary spatially[3]. While sabkhas are a dominant topographic feature in the Arabian Peninsula and North Africa, particularly in the coastal areas, these distinctive soils are widely dispersed across the globe (Fig. 1a).

Sabkhas are classified into two types: coastal and inland based on their origin, solute sources, and hydrological processes[7]. Coastal sabkhas, typical in shallow marine shelves (e.g., Arabian Gulf), are directly influenced by seawater influx[8]. In contrast, inland sabkhas are associated with artesian flow from shallow aquifers, driven by high permeability and positive hydraulic gradients[9–11]. These brines mix with present-day aquifers and differ from the marine deposition processes (subtidal to supratidal) that form coastal sabkhas[12,13]. Due to their intricate geological history, sabkhas exhibit significant vertical and lateral heterogeneity. Therefore, a thorough understanding of near-surface seismic wave behavior and its influencing factors is crucial for various applications, including geotechnical uses, static corrections, time-depth conversion, and determining the depth of the water

[1]Department of Earth Sciences, Khalifa University, Abu Dhabi, United Arab Emirates. [2]Department of Geosciences, King Fahd University of Petroleum and Minerals, Dhahran, Saudi Arabia. [3]Graduate School of Frontier Sciences, The University of Tokyo, Tokyo, Japan. ✉email: ak.eleslambouly@gmail.com; 100059651@ku.ac.ae

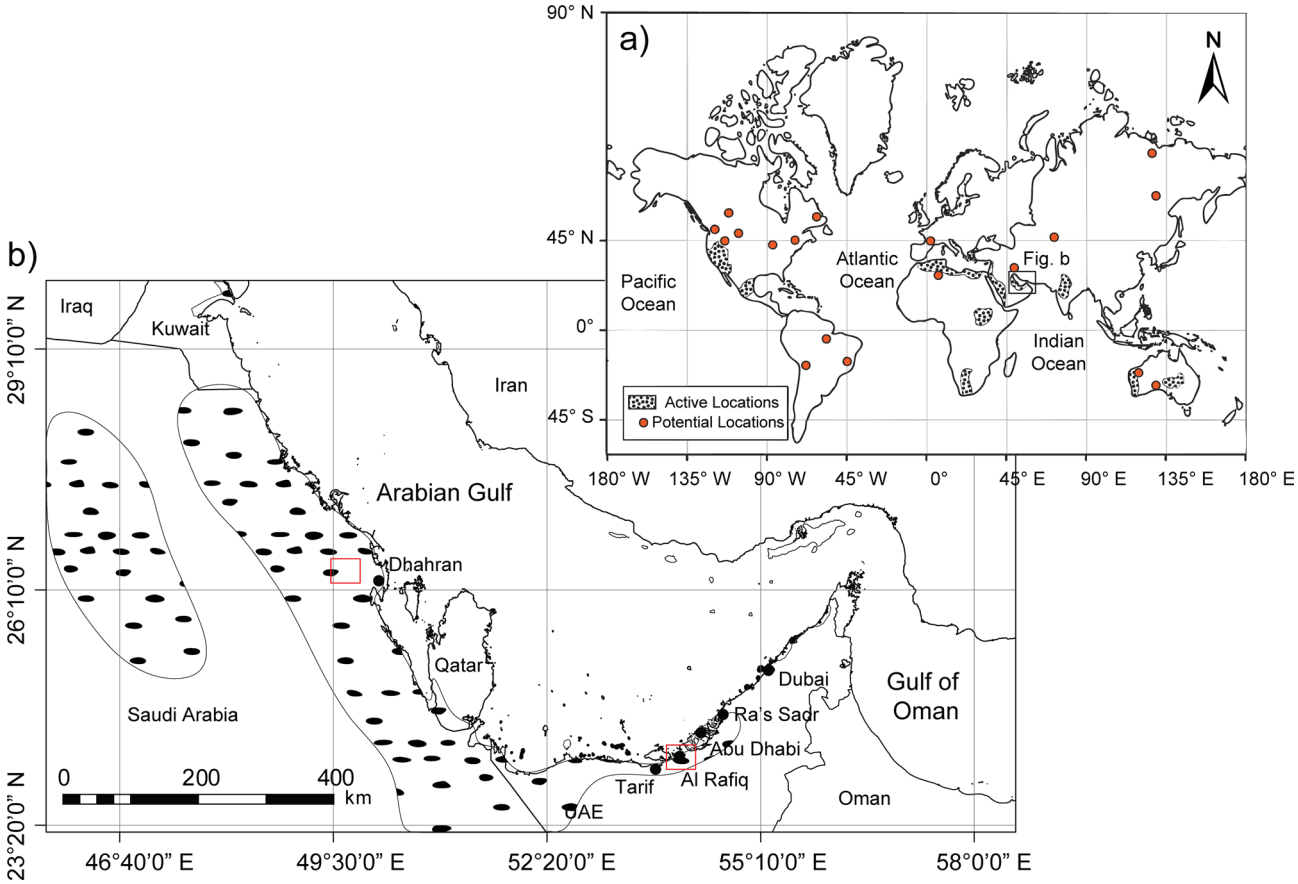

Fig. 1. Schematic maps illustrate the sabkha soil distribution globally and along the Arabian Gulf. (**a**) The map highlights the coastal and inland sabkhas distribution and potential locations, the global sabkhas environments compiled after Al-Amoudi and Abduljauwad[4]. (**b**) Regional map of sabkha distribution along the Arabian Gulf. Highlighted areas represent the extent of sabkha soils. The sabkha locations along the Arabian Gulf are adopted after Al-Amoudi, et al.[5]. Red rectangular boxes indicate the two study areas: Coastal Sabkha of Abu Dhabi (CSAD) in the UAE and Sabkha Jayb Uwayyid (SJUW), located west of Dhahran city in eastern Saudi Arabia. Both panels highlighted locations are populated from the published extents in Al-Amoudi and Abduljauwad[4] and[5]and compiled in ArcGIS Pro Software[6], The figures were created in ArcGIS Pro Software[6] (V3.6, https://www.esri.com/en-us/arcgis/products/arcgis-pro/overview), a commercial geographical information system software from ESRI.

table. From a geotechnical perspective, sabkha soils pose numerous challenges owing to their unique chemical and physical characteristics[14,15]. The most dominant problem with sabkha properties is the compressibility of their sediments, which have a high potential to collapse due to salt dissolution. Additionally, hydration and dehydration of unstable gypsum within sabkha deposits can cause substantial volumetric changes, potentially damaging overlying infrastructure[16,17].

The seismic properties of sabkha vary with the maturity degree of sabkha, as it influences the amount of evaporitic minerals and water content within the uppermost interval[18]. Gates, et al.[19] used seismic refraction at the Texas Salt Flats and found compressional waves (V_P) in the ranges 910-914 m/s and 1890-1981 m/s above and below the water table, respectively. Al-Husseini, et al.[20] obtained a Poisson's ratio of 0.4 after performing seismic noise analysis in the sabkhas in northeastern Saudi Arabia. Robinson and Al-Husseini[21] also used seismic noise analysis to study the sabkhas of Rub Al-Khali in southeastern Saudi Arabia and reported an average V_P and shear waves (V_S) of 370 m/s and 190 m/s, respectively, above the water table. While the average V_P and V_S below the water table are 1520 m/s and 420 m/s, respectively. Adel, et al.[22] used multi-component seismic refraction to characterize the sabkhas in the eastern Gulf of Suez. They reported V_P and V_S in the ranges 540–1000 m/s and 200– 250 m/s, respectively, above the water table. Al-Shuhail and Al-Shaibani[23] used seismic refraction profiling to study the Aziziyah and Ar-Riyas sabkhas in eastern Saudi Arabia. They found the average V_P above the water table is 300 m/s in both sabkhas. Below the water table, they obtained an average V_P of 1775 m/s in the Aziziyah sabkha and 2150 m/s in the Ar-Riyas sabkha. Furthermore, Al-Shuhail and Al-Shaibani[24] studied the inland Sabkha Jayb Uwayyid (SJUW) in eastern Saudi Arabia using seismic refraction profiling. They found that the V_P ranged from 500 to 700 m/s above the water table and from 2100 to 2500 m/s below it. Additionally, they identified the bedrock at a depth of 100 m with an average V_P of 3350 m/s. El-Hussain, et al.[25] conducted seismic refraction and MASW (Multichannel Analysis of Surface Waves) surveys along a 3000 m length profile

parallel to the coastline of the sabkha deposit at the port of Duqm in the Sultanate of Oman. They identified three distinct subsurface layers within the shallow zone. The uppermost layer exhibited average V_P and V_S of 400 m/s and 250 m/s, respectively. The intermediate layer demonstrated average V_P and V_S of 1300 m/s and 525 m/s, respectively. The deepest of the three layers was characterized by average V_P and V_S of 2450 m/s and 750 m/s, respectively. Al-Heety, et al.[26] conducted a MASW study at the Mussafah Channel sabkha, located southwest of Abu Dhabi City. Their findings revealed a near-surface dry layer characterized by a low V_S of 180 m/s. Beneath this layer, a water-saturated layer was identified, exhibiting V_S values ranging from 220–360 m/s. At a depth of 6 m, a third layer was delineated, with V_S values between 360-750 m/s, extending to a depth of 17 m. A fourth layer was detected at a depth of 20 m, with V_S values below 750 m/s, and was interpreted to consist of lithified rock.

In a recent study by Eleslambouly, et al.[27], they discussed the variations in V_P in CSAD and SJUW using high-resolution and conventional seismic refraction profiles in each sabkha, where the presence of evaporitic facies can lead to high V_P in the weathered layer, this is followed by a partially saturated zone characterized by V_P values lower than 950 m/s. Below this zone, a third fully saturated zone was identified with V_P exceeding 1800 m/s. Moreover, no previous studies focused on obtaining and integrating V_P and V_S relationship from surface seismic data and their properties in sabkha soils. The integration of V_P and V_S can provide a more insightful interpretation of the fluids and lithology properties, providing powerful imaging for the near subsurface of both sabkhas. This study aims to resolve the complexity associated with near-surface geology, which is mostly not captured by traditional seismic techniques. Moreover, this study aims to integrate seismic anisotropy and attenuation parameters with seismic velocity measurements to enhance the characterization of both inland and coastal sabkha environments.

Two seismic profiles were acquired to generate detailed 2D images of the subsurface properties within two of the most extensive sabkha environments in the Arabian Gulf (Fig. 1b): the Coastal Sabkha of Abu Dhabi (CSAD) and the Inland Sabkha of Jayb Uwayyid (SJUW). An integrated workflow was employed (Fig. 2), incorporating two widely utilized near-surface geophysical techniques: seismic refraction, for the estimation of V_P, and MASW, for the estimating V_S within the subsurface. Headwave arrivals and surface wave dispersion curves were independently inverted to derive both V_P and V_S The V_P/V_S ratio was subsequently computed to extract additional information regarding subsurface conditions. Furthermore, seismic analyses were conducted to assess seismic attenuation ($Q_P{}^{-1}$) and to V_P anisotropy to the fluid presence and properties in the subsurface. The results not only refine and corroborate previous interpretations but also provide novel insights into the elastic and anelastic properties of sabkha environments, thereby enhancing our understanding of their influence on seismic wave propagation.

Study areas and general geology

This study examines two of the largest Holocene sabkhas in the Arabian Gulf: the supratidal zone of the mature CSAD and the immature SJUW (Fig. 1b). The CSAD is located on the southern coastline of the Arabian Gulf in the United Arab Emirates (UAE), extending over 150 km from Ra's Sadr to Tarif, and extends up to 15 km inland. The supratidal zone holds the thickest sabkha deposits and a fully formed sequence of evaporitic facies[18] and is underlain by a thin hardground (20-50 cm), mainly consisting of cemented skeletal fragments bound together

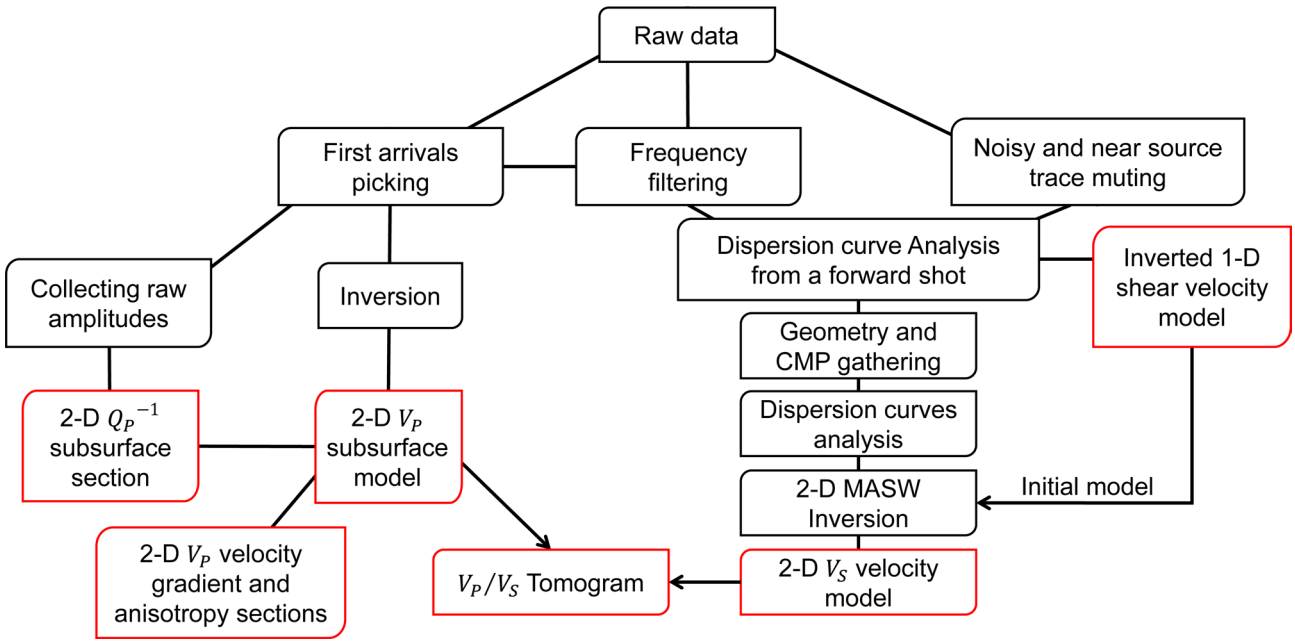

Fig. 2. Workflow for seismic data processing and subsurface modeling. A flowchart illustrating the processing steps applied to the collected data to obtain a 2-D subsurface for V_P, V_s, V_P/V_S, Q_P^{-1}, and anisotropy models.

by calcitic cement, which varies in degree and thickness with a trend shallowing in seaward direction[28]. The sabkha overlies a complex stratigraphic sequence of Holocene sediments that have undergone multiple episodes of deposition and erosion[29]. The sediment succession beneath the sabkha remains unexplored; however, several studies have investigated the outcrops of the underlying formations[29–31]. Directly beneath the Holocene sabkha deposits lies the Ghayathi Formation, composed of Late Pleistocene to early Holocene aeolian dune sands. This formation consists of pale brown aeolianite and an unconsolidated palaeodune system, characterized by poorly cemented carbonate sediments[32]. Underlying the Ghayathi Formation is the Late Pleistocene Marawah Formation, which is predominantly composed of carbonate rocks[33]. Beneath this, the Middle to Late Pleistocene Madinat Zayed Formation comprises lightly consolidated quartzose red and brown aeolian dune sands, with cementation ranging from poorly to fully cemented by gypsum[31]. The dominant subsurface facies beneath the sabkha are expected to consist of alternating siliciclastic palaeodunes and carbonate deposits, reflecting rapid sea-level fluctuations during the Quaternary[33]. The regional bedrock of the Abu Dhabi Emirate is of Late Miocene age and primarily consists of gypsiferous carbonate and mudstone lithologies[34]. This bedrock is exposed at select locations due to tectonic uplift, particularly toward the Al Ain region, and exhibits features indicative of erosional and karstic processes[35,36].

The second study area is the inland SJUW, located in the Eastern Province of Saudi Arabia, west of Dhahran City (Fig. 1b). The SJUW is among the largest inland sabkhas on the Arabian Peninsula. It is bordered by peripheral dunes and sand sheets, and its surface features patches of thin salt beds, which are partially covered by windblown sands[37]. The sabkha sediments predominantly consist of unconsolidated, poorly sorted quartzose sands, with fine- to medium-grain gypsum occurring both above and below the water table[38]. A bedded halite deposit is present at depths ranging from 2.8 to 4 m, with a thickness between 0.3 to 3.7 m, extending 5 km in length, and 1.8 km in width[39,40]. The Holocene sabkha deposits overlie a thick Pleistocene sequence composed of alternating layers of sand, limestone, and shale[7,39]. The underlying bedrock beneath is the Early Miocene Hadrukh Formation, which outcrops at the northern margin of the sabkha and is characterized by calcareous sandstone in its uppermost section[41].

Materials and methods

Dataset

This study utilized two seismic profiles with evenly spaced geophones to acquire high-lateral-resolution near-surface geophysical profiles. The CSAD receiver array was rolled along in successive deployments to extend the coverage length while preserving geometry (Figs. 3a and 3b). Acquisition parameters for the CSAD and SJUW surveys are summarized in Table 1, and the acquired gathers geometry is illustrated in Supplementary Fig. 1.

Seismic refraction processing and compressional wave velocity inversion

The acquired seismic refraction data were initially subjected to filtering and muting to eliminate noisy traces and enhance the identification of first-arrival headwaves (Fig. 4). First-arrival travel times were manually picked from the shot gathers and used as input for seismic tomography inversion. This inversion technique utilizes

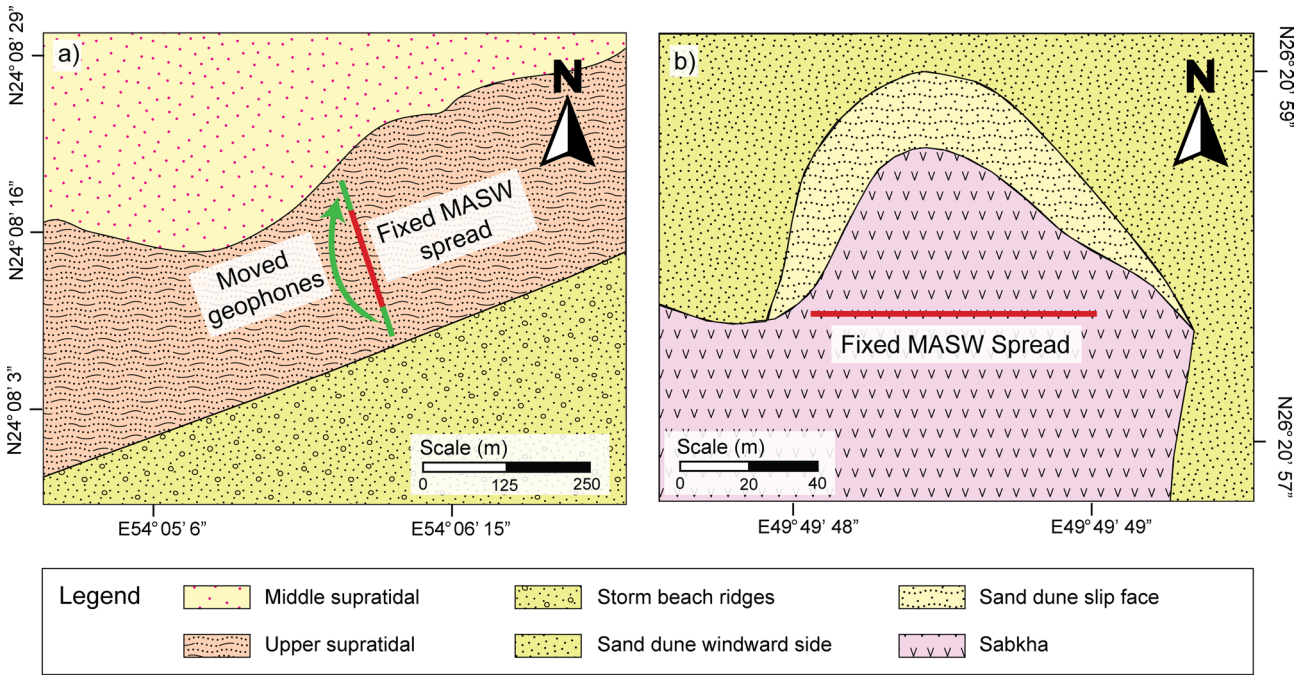

Fig. 3. Surface geology along with seismic acquisition layout at the CSAD and SJUW sites. (**a**) Map of the CSAD site showing the fixed MASW spread and the moved geophone locations. (**b**) Map of the SJUW site showing the fixed MASW spread deployed.

Parameter	CSAD	SJUW
Number of geophones	96 (4.5 Hz) fixed + 24 moved	72 (14 Hz) fixed
Geophone spacing	2 m	2 m
Total covered length	238 m	142 m
Seismic source	12 kg sledgehammer	90 kg weight-drop
Shot spacing	6 m	2 m
Number of stacked shots	3 per location	5 per location
Number of acquired shots	43 shots + 4 offset shots	64 shots
Plate size	20 × 20 cm metallic plate	
Recording length	1 s	
Sampling rate	0.5 ms	

Table 1. Seismic surveys acquisition parameters for CSAD and SJUW.

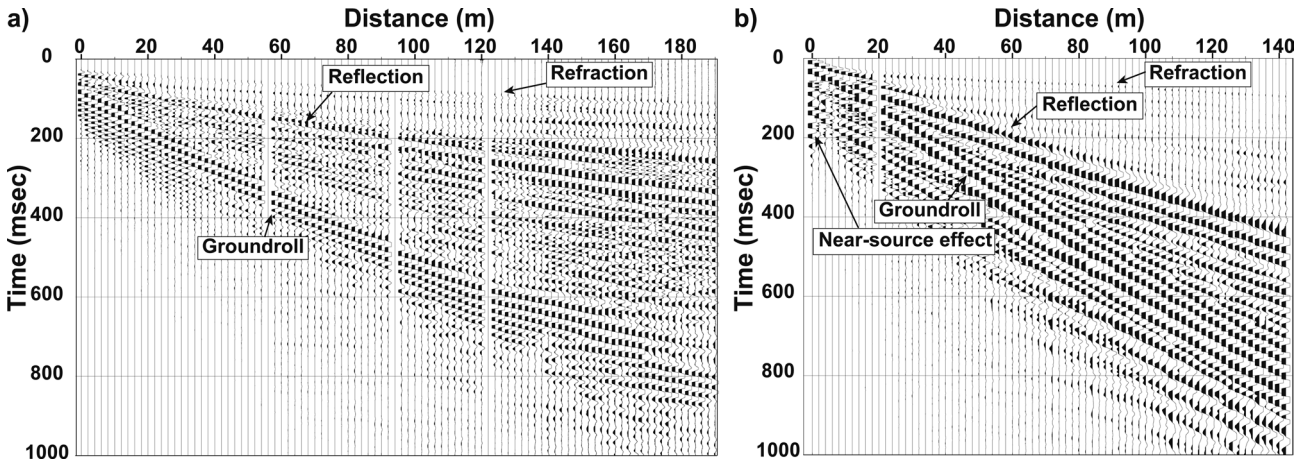

Fig. 4. Raw shot gathers waveform from seismic acquisition at CSAD and SJUW. (**a**) CSAD, showing offset shot at −10 m with identifiable groundroll, reflection, and refraction phases. (**b**) SJUW, showing a forward shot at 0 m with additional near-source effects. Noisy geophones have been muted to enhance signal clarity.

arrival times without requiring predefined subsurface layering or directional assumptions for the subsurface V_P gradients[42,43].

To ensure data quality and reduce noise, a reciprocal test was applied to the travel-time dataset. A squared mesh with a cell thickness of 0.5 m was built, and a synthetic initial model was generated using a linear velocity gradient ranging from 250 m/s to 2600 m/s, consistent with dry to saturated sabkha sediments reported regionally[23,24,27]. Reciprocal shots were used to constrain timing errors. Ray paths were computed based on this initial model, and predicted travel times were compared with observed values. The residuals between predicted and observed travel times were iteratively minimized using a least-squares inversion approach over 10 iterations (Supplementary Fig. 2), resulting in a final V_P tomogram for each sabkha site.

To address areas not covered by ray paths, an extrapolation technique based on nearest-neighbor interpolation was applied. While this extrapolated section aids in matching the dimensions of the V_P tomograms for subsequent analysis should be interpreted with caution due to the lack of direct ray coverage. Additionally, the vertical gradient of V_P was computed for each cell using a finite difference approach, expressed as V_P/dz, where dz is the cell thickness. These gradient profiles provide enhanced insight into lateral and vertical variations in V_P, facilitating the identification of layer boundaries and zones of significant velocity change[44].

Seismic anisotropy

To assess seismic anisotropy in the subsurface, the P-wave anisotropy coefficient was calculated as the ratio of horizontal to vertical V_P, expressed as V_x/V_y, where V_x and V_y represent the horizontal and vertical components of V_P, respectively[45], using first-arrival travel-time data acquired along the refraction profile. In this framework, each model cell is defined by both the vertical V_P (V_y) and the anisotropy coefficient[46]. We assume a transversely isotropic (TI) model as an initial assumption for typical sabkhas with horizontally layered evaporite-sand sequences and shallow facies. In such a setting, seismic wave velocities are considered isotropic within horizontal planes but vary with depth, with the symmetric axis oriented vertically due to the horizontal layering.

Horizontal velocities (V_x) were derived directly from the seismic refraction tomography, while vertical velocities (V_y) were constrained during the inversion using geological priors and regularization. The inversion initially assumed isotropy for the first one to two iterations to stabilize the velocity model. From the third iteration

onward, anisotropy was introduced by allowing simultaneous adjustment of both velocity components and the anisotropy coefficient (V_x/V_y), with optimization guided by minimization of residuals between observed and modeled travel times. Each tomographic cell was characterized by a vertical V_P value and its associated anisotropy coefficient, enabling the capture of localized directional velocity contrasts.

Given the lack of intersecting fractures or multi-azimuthal features in sabkha settings, higher-order anisotropy (e.g., orthorhombic) was not considered, and the assumption of transverse isotropy was maintained throughout the analysis. Departures from TI symmetry are recognized as a potential source of modeling uncertainty, particularly in the absence of well log constraints. Nonetheless, this joint inversion strategy enhances sensitivity to directional wave propagation and enables a more robust delineation of near-surface anisotropic structures, which are critical for interpreting the lithological and hydrological heterogeneity of sabkhas.

Seismic attenuation ($Q_P{}^{-1}$)

To determine the spatial distribution of compressional attenuation, often quantified by the inverse quality factor $Q_P{}^{-1}$. We applied an attenuation tomography approach based on the procedure proposed by Aki and Richards[47]. Prior to attenuation analysis, geometrical spreading compensation was applied to the amplitudes to isolate the effects of attenuation (scattering and intrinsic attenuation). This analysis was conducted after generating the 2D V_P tomograms and computing the associated ray coverage. Amplitude data were extracted using the first-arrival picks and a time window centered at the arrival time, with a window length approximately equal to one average wavelength. The amplitude decay due to attenuation can be expressed using the following relationship:

$$A\,(t) = A_0 \cdot e^{-\pi f t/Q_P} \tag{1}$$

where $A\,(t)$ is the geometrically corrected amplitude at travel time t, A_0 is the amplitude of the source, f is the frequency, A log-linear regression of $\ln A(t)$ versus t was performed at each receiver to determine the attenuation coefficient $\alpha = \pi f/Q_P V_P$, and hence:

$$Q_P{}^{-1} = \frac{\alpha V_P}{\pi f} \tag{2}$$

$Q_P{}^{-1}$ represents the combined intrinsic plus scattering attenuation as we correct for the geometrical spreading; the time window is approximately one wavelength, centered on the first arrival. The resulting $Q_P{}^{-1}$ values were then mapped along the ray paths using the previously derived V_P tomogram, yielding a depth-resolved attenuation model. This approach enables the identification of zones with elevated seismic energy loss, which are often associated with fluid saturation, lithological heterogeneity, or structural complexity.

MASW data processing and V_S inversion

To enhance lateral resolution and achieve greater investigation depths, a non-conventional acquisition setup was employed using fixed geophones along extended survey lines. This configuration enabled the recording of low-frequency surface waves, which are essential for deep shear-wave penetration. The Common Midpoint Cross-Correlation (CMPCC) technique was applied to extract dispersion information and construct a 1-D V_S profiles at each geophone location. The recorded data underwent several key processing steps to ensure high-quality inversion results (Fig. 2). Initially, noisy and near-source traces were removed to eliminate high-frequency artifacts that degrade the quality of the dispersion spectra. A representative dispersion spectrum was computed from a forward-shot gather using a linear frequency–wavenumber (F-K) transform (slowness vs. frequency; Fig. 5). This spectrum served as the input for MASW inversion, leading to the generation of a 2-D V_S tomogram.

Active MASW techniques were used to analyze Rayleigh surface waves and produce both 1-D and 2-D V_S profiles. Since shear-wave velocity is directly linked to the elastic properties (stiffness) of the ground, it serves as a critical parameter for geotechnical characterization[48]. A 1-D phase velocity curve was manually picked from the dispersion spectrum, and iterative inversion was performed to minimize the root mean square (RMS) error of V_S. A seven-layer model was applied for both CSAD and SJUW, with ten inversion iterations guided by existing geological knowledge and seismic refraction results[27] (Figs. 6a and 6b). The initial velocity model was based on a theoretical phase velocity curve, assuming increasing V_S with depth. The inverted curves showed good agreement with the observed data and yielded an average V_S values for each layer (Figs. 6c and 6d). The depth of penetration achieved in the inverted models reflects the low-frequency content captured due to the long-offset acquisition geometry. To construct the 2D V_S tomogram, the CMP cross-correlation technique was applied to the MASW dataset[49]. CMP gathers were generated by cross-correlating waveform data and were collected every 2 m, matching the geophone spacing (Supplementary Fig. 3). These gathers (Supplementary Figs. 4 and 5) were transformed into dispersion spectra (Supplementary Figs. 6 and 7), from which 1-D dispersion curves were picked at each CMP location. CSAD exhibited greater variability due to its more complex subsurface conditions (Supplementary Figs. 8). The picked phase velocity curves were inverted using a least-squares approach, with ten iterations applied to each dataset, after which improvements were marginal[50]. The RMS error decreased rapidly within the first five iterations and stabilized between 20–30 m/s, which is considered acceptable in the absence of borehole calibration (Supplementary Fig. 9).

Results

Velocity tomograms and V_P/V_S ratio

The 2-D V_S tomograms produced from the MASW technique represent an interpolation of V_S along each point across the profile (Fig. 7), extending to depths of >100 m at CSAD (Fig. 7a) and ~65 m at SJUW (Fig. 7b). In the shallowest section of the CSAD tomogram, V_S begin at approximately 286 m/s, thinning toward the coastline.

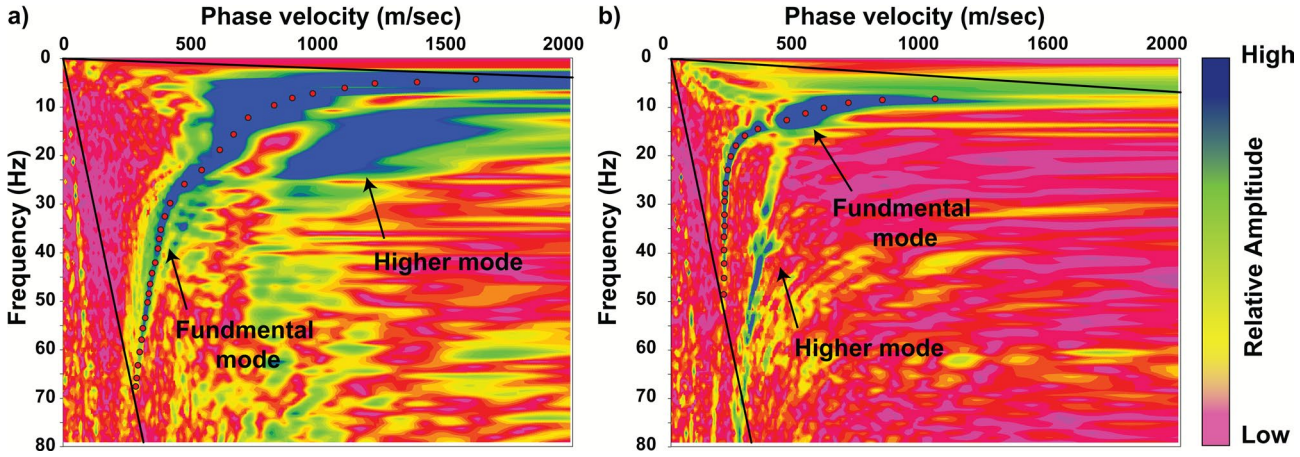

Fig. 5. Dispersion spectra from MASW analysis of CSAD and SJUW shot gathers. (**a**) CSAD and (**b**) SJUW. Dispersion spectra retrieved after transforming the shot gathers in Figure 4, overlain with picked curves of the fundamental modes (red points). The color palette represents the relative amplitude intensity of the dispersion spectra. The black lines indicate the theoretical phase-velocity window bounds for picking the fundamental mode.

High V_S values are observed in the northwestern portion of the profile, reaching a maximum of 374 m/s. A distinct ridge feature is evident between 45 and 105 m along the profile, characterized by increased V_S values. The maximum V_S in the CSAD profile is 1831 m/s at an approximate depth of 100 m. In contrast, the SJUW V_S tomogram exhibits smoother contours in the upper layers, with significantly lower V_S values in the shallowest section (157 m/s) compared to CSAD. The upper portion of the SJUW profile appears nearly horizontal, with minimal lateral variation. However, the deeper sections reveal vertical zones of reduced V_S, resembling pillar-like structures. Overall, the SJUW tomogram demonstrates a gradual increase in V_S with depth.

The V_S tomograms obtained from MASW (Fig. 7) were depth-limited to match the depth of penetration of the seismic refraction V_P tomograms, enabling the computation of the V_P/V_S ratio (Figs. 8 and 9). In the CSAD profile, a near-surface zone of low V_P is observed, thinning toward the coastline (Fig. 8a). This is followed by a second zone exhibiting a similar spatial trend but characterized by a higher V_P gradient (Fig. 8b). The deeper section reveals a third zone where V_P exceeds 1500 m/s, with a smaller gradient contrast compared to the shallower layers. The corresponding V_S tomogram (Fig. 8c) displays a similar low-velocity zone near the surface, also thinning toward the coastline. This is succeeded by a second zone where V_S begins to vary in thickness, and a third zone at approximately 15 m depth, where V_S exceeds 760 m/s. The V_P/V_S ratio section (Fig. 8d) reveals a near-surface zone with values not exceeding 1.5, following the same pinching-out trend observed in the V_P and V_S tomograms. This is followed by a zone where the ratio ranges between 1.5 and 2.5, extending a depth of up to 8 m. A third zone exhibiting the highest V_P/V_S ratio with maximum values of 3.4 in the northwestern, seaside portion of the profile. At greater depths, the ratio decreases again, stabilizing at a value of approximately 2.5 at a depth of around 27 m.

In contrast, the V_P tomogram for the SJUW profile (Fig. 9a) reveals a shallow uppermost zone of nearly uniform thickness, extending to approximately 5 m depth, where V_P values remain below 1000 m/s. This zone is associated with a high-velocity gradient near the surface, particularly within the upper 1.5 m (Fig. 9b). Beneath this, a second zone is characterized by V_P values ranging from 1000 to 1800 m/s, exhibiting an almost horizontal geometry and a pronounced velocity gradient along its upper boundary. A third, deeper layer displays V_P values between 1800 and 2500 m/s, with both lateral and vertical velocity contrasts evident within this zone. The corresponding V_S tomogram (Fig. 9c) shows a horizontally layered structure with a steady increase in V_S with depth. The shallowest zone contains low V_S values (<380 m/s) within the upper few meters, followed by a second zone where V_S ranges from 380 to 760 m/s. A third zone, located at approximately 12.5 m depth, exhibits V_S values exceeding 750 m/s. The V_P/V_S ratio section (Fig. 9d) reveals a thin, near-surface zone, extending to about 0.8 m depth, where the ratio does not exceed 2.5. This is followed by a vertically oriented zone with V_P/V_S ratios ranging from 3 to 4.5, concentrated in the middle-right portion of the section and extending from approximately 5 m depth into the deeper parts of the tomogram. In the lowest parts of the section, the ratio gradually decreases again, stabilizing at approximately 2.5 at a depth of around 17 m.

Seismic anisotropy and attenuation ($Q_P{}^{-1}$)

Seismic anisotropy and attenuation results, derived from the inversion of the V_P tomograms for both sabkha sites are presented in Figure 10. Anisotropy is expressed as the V_p ratio V_x/V_y, which approximates directional velocity contrast under the assumption of transverse isotropy. The anisotropy section for CSAD (Fig. 10a) reveals significant directional variations in V_P within the upper 5 m, indicating strong near-surface heterogeneity. A second zone, between 5 and 10 m depth, exhibits reduced anisotropy, while depths beyond 15 m display a more uniform and homogenous anisotropic pattern, suggesting consistent subsurface properties at greater depths. In contrast, the SJUW anisotropy section (Fig. 10b) shows pronounced directional V_P variations near the surface,

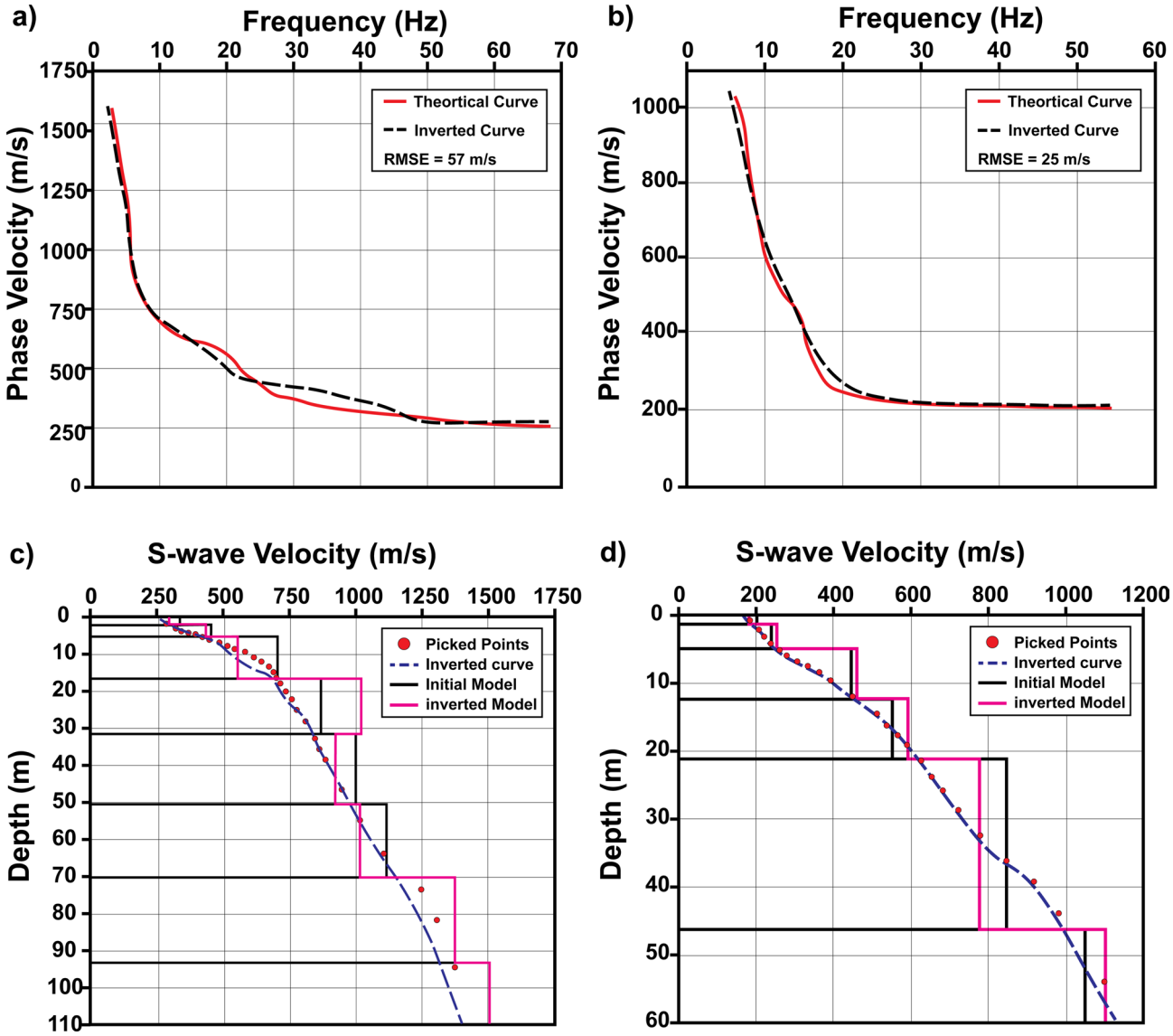

Fig. 6. Comparison of the initial 1-D shear wave velocity (V_S) and inversion results at CSAD and SJUW. (**a**, **b**) Observed versus inverted dispersion curves at the CSAD and SJUW, respectively. Red lines represent theoretical curves, and black dashed lines indicate the inverted fits, along with their associated RMSE values. (**c**, **d**) Step plots of initial (black) and inverted (pink) 1-D V_S profiles for CSAD and SJUW, respectively, highlighting layer-specific velocity adjustments through inversion.

followed by more vertically oriented anisotropic changes in the middle section. The deeper layers exhibit complex anisotropic behavior, reflecting a more heterogeneous subsurface structure.

The Q_P^{-1} profile of the CSAD (Fig. 10c) shows the highest ${Q_P}^{-1}$ values (up to 0.05) near the surface, particularly in the northwestern portion, are characterized by high attenuation magnitudes (0.013-0.05) to a depth of approximately 15 m. Below this depth, ${Q_P}^{-1}$ decreases markedly, with more uniform and lower ${Q_P}^{-1}$ values (indicated by blue regions), suggesting reduced seismic energy loss in the deeper subsurface. Conversely, the SJUW attenuation profile (Fig. 10d) displays a thin (<1 m), localized zone of high attenuation near the surface. Between 5 and 15 m depth, a distinct band of elevated ${Q_P}^{-1}$ indicates significant energy dissipation. Below 15 m, attenuation decreases, with more uniform low ${Q_P}^{-1}$ values, indicating reduced energy absorption at greater depths. Within the upper ~10-15 m at both sites ${Q_P}^{-1}$ ranges between 0.013-0.05, highlighting the highest attenuation regions.

Discussion

V_P Are commonly used to map the groundwater levels due to their ability to propagate through both solid and fluid media[51,52]. V_P is highly sensitive to the presence of fluids in the subsurface, as fluid saturation reduces the compressibility of the rock matrix, thereby increasing V_P[53]. Even a minimal gas content can significantly reduce V_P, making V_P highly sensitive to fluid saturation levels[54]. In contrast, V_S propagate only through

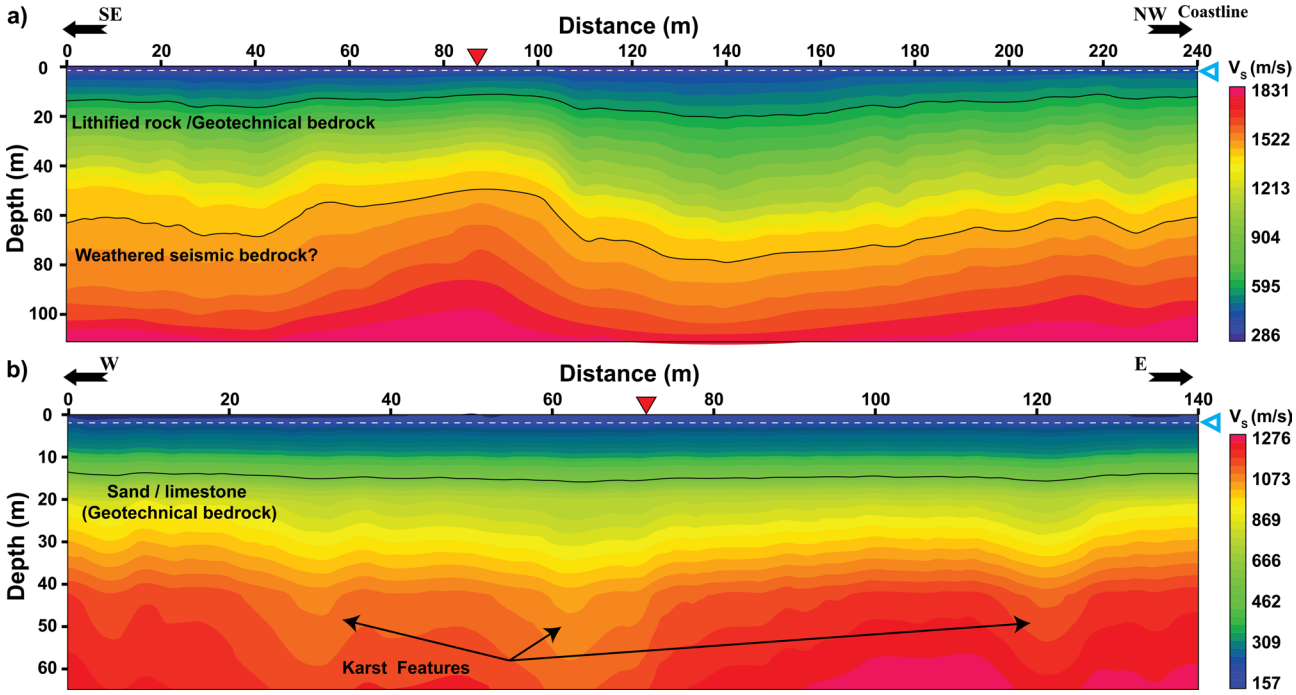

Fig. 7. 2-D V_S tomograms obtained from the MASW data for (**a**) CSAD and (**b**) SJUW sites. Red triangles denote the locations of the initial 1-D V_S models derived from forward shots; blue triangles mark the inferred water table. The high V_S values at CSAD are attributed to lithified rock, while SJUW reveals karstic features and a sand/limestone bedrock.

solid materials and are therefore less affected by fluid content[55]. Fluid saturation primarily influences the bulk modulus of the rock matrix, while V_S remains relatively stable unless the fluids significantly alter the rock's shear strength. As a result, variations in V_S are more indicative of changes in the mechanical properties of the rock matrix rather than fluid saturation.

The V_P/V_S ratio serves as a critical parameter for distinguishing between lithologies and fluid types in the subsurface. In saturated sediments, this ratio typically increases due to the rise in V_P while V_S remains relatively unchanged. In shallow, unconsolidated sediments, a high V_P/V_S ratio often indicates full saturation, whereas a low ratio suggests dry or partially saturated conditions. Laboratory investigations by Conte, et al.[56] demonstrated that in dry unconsolidated sediments (e.g., sands and silts), the V_P/V_S ratio can be as low as 1.45, reflecting dependence on the shear modulus. As saturation increases to approximately 90%, the ratio rises sharply, reaching values of up to 4.5, depending on the sediment type and saturation level, driven by increases in the bulk modulus. Furthermore, Pasquet, et al.[57] demonstrated the use of V_P/V_S derived from seismic tomography and surface wave analysis for characterizing the near-surface and estimating the water table depth. Their study showed that combining surface-wave dispersion inversion with V_P tomography enables effective estimation of the V_P/V_S ratio, providing detailed insights into lateral variations in shallow subsurface layers.

The low-frequency components (<10 Hz) observed in the dispersion velocity spectra (Fig. 5) are primarily attributed to the extended profile lengths, which facilitate the propagation of surface waves over greater distances. This propagation leads to the progressive attenuation of higher-frequency energy due to both intrinsic and scattering losses[58,59]. As a result, these low-frequency signals provide valuable insights into V_S at greater depths, albeit with reduced vertical resolution, thereby highlighting only large-scale subsurface structures[60]. While this approach is effective for identifying major anomalies, it lacks the resolution necessary to detect finer-scale features . In this study, the geotechnical bedrock, defined by V_S values exceeding 760 m/s[61] was identified at depths of approximately 15 m in the CSAD profile and 12.5 m in the SJUW profile (Fig. 7). Additionally, in the CSAD profile, a deeper bedrock horizon was delineated at depths between 60 and 70 m, where V_S exceeds 1500 m/s[34] (Fig. 7a). The low topographic elevation of the area suggests it functions as a regional discharge zone for deeper aquifers, making it particularly susceptible to dissolution processes driven by continental hydrological cycles[2]. In contrast, the bedrock in the SJUW was not detected within the 65 m depth range of the current survey. Previous work by Al-Shuhail and Al-Shaibani[24] identified the bedrock at depths ranging from 100 to 120 m. Furthermore, vertical low-V_S anomalies observed at approximately 50 m depth in the CSAD profile (Fig. 7b) are interpreted as localized subsurface cavities or karstic features. This interpretation is based on the anomalously reduced shear-wave velocity signature, its confined lateral extent, and its position within carbonate-evaporite lithologies that are prone to dissolution. Karst development is common across the Arabian Gulf coastal zones due to the solubility of Eocene formations and fluctuating groundwater conditions, and has been extensively reported in nearby regions[62–65].

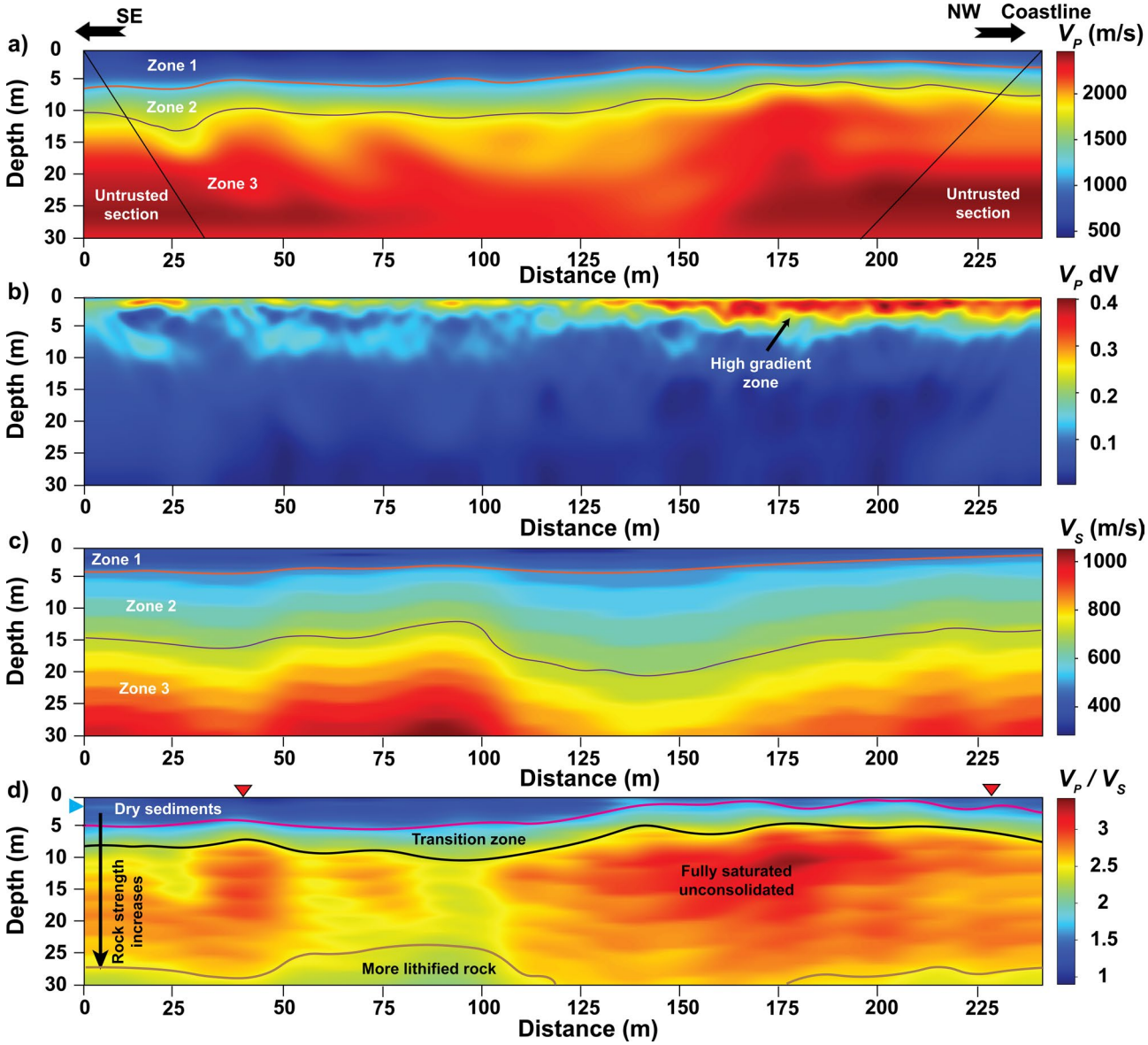

Fig. 8. 2D subsurface sections from CSAD. a) V_P tomogram obtained from seismic refraction data. The zones in the SE and NW corners, marked by black oblique lines, indicate areas where data points have been extrapolated to the nearest neighbor and should be regarded as unreliable. (**b**) velocity gradient (dV_P). (**c**) V_S tomogram cropped to match V_P penetration depths. (**d**) Computed V_P/V_S section from obtained tomograms in **a** and **c**, the red triangles refer to high-resolution locations in Eleslambouly, et al. [27]. The blue triangle represents the water table level based on shallow borehole observations.

Additionally, a near-surface low-velocity zone in CSAD is evident in both V_P (Fig. 8a) and V_S (Fig. 8c) tomograms, characterized by V_P values below 428 m/s and V_S values below 261 m/s. This zone is interpreted as dry, unconsolidated sediments associated with the sabkha's evaporitic facies and shallow hardground, which progressively thins toward the coastline. The CSAD profile exhibits higher V_S compared to SJUW, primarily due to the presence of a consolidated hardground layer. The thickness and degree of cementation of the hardground increase seaward[18], indicating a stiffer soil structure relative to the uppermost sediments of SJUW. Beneath the sabkha deposits at CSAD, the V_S values in the underlying aeolian sands reach approximately 568 m/s, suggesting a dense, homogeneous sand lithology that is not lithified rock[66]. A pronounced V_P gradient is observed in the shallowest part of this zone (Fig. 8b), within a 1 - 3 m thick layer, and is attributed to lithological and hydrological variations influenced by sea water flux changes. Furthermore, seismic anisotropy in this upper zone exhibits high variability, likely due to significant contrasts in the thickness of the evaporitic facies[67]. In contrast, deeper sections of the profile exhibit reduced anisotropy, indicating more homogeneous subsurface layers with less structural complexity beneath the sabkha sediment.

In contrast to the CSAD profile, the SJUW profile is characterized by more homogeneous subsurface layers, with sub-horizontal bedding and minimal velocity contrasts (Figs. 9a and 9b). The 2D anisotropy section (Fig.

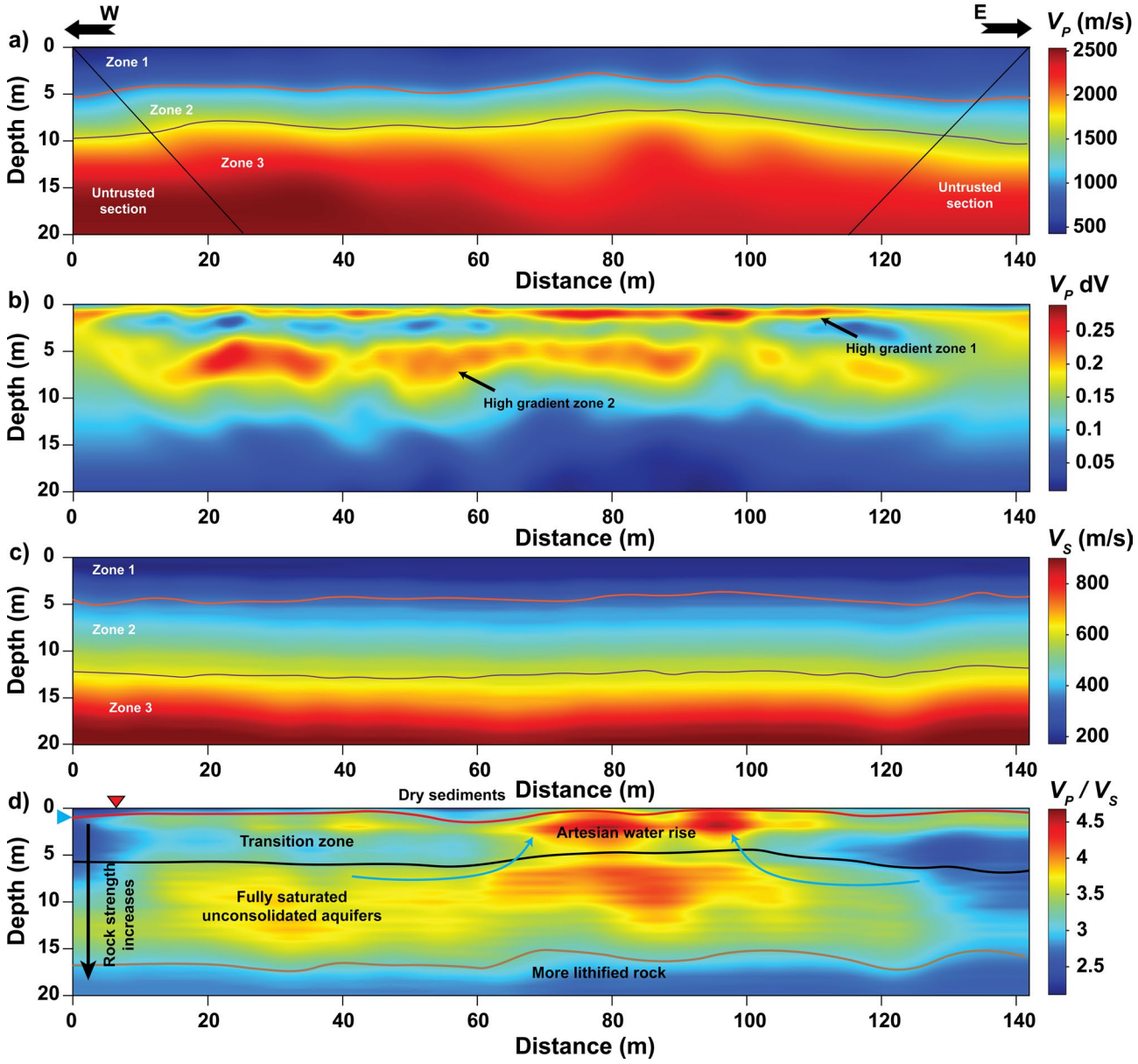

Fig. 9. 2D subsurface sections from SJUW.**a**) V_P tomogram obtained from seismic refraction data. The zones in the SE and NW corners, marked by black oblique lines, indicate areas where data points have been extrapolated to the nearest neighbor and should be regarded as unreliable. (**b**) velocity gradient (dV_P). (**c**) V_S tomogram cropped to match V_P penetration depths. (**d**) Computed V_P/V_S section from obtained tomograms in **a** and **c**, the red triangles refer to high-resolution locations in Eleslambouly, et al. [27]. The blue triangle represents the water table level based on shallow borehole observations. Blue curved arrows refer to the rise of the water as a result of an artesian effect.

10b) reveals an uppermost zone extending to ~1.5 m depth, with moderate lateral variations, followed by a zone up to 10 m where vertical velocity gradients dominate. This transition corresponds to a second lithological layer with distinct properties. At greater depths (>10 m), increased anisotropy and elevated V_P/V_S ratios (Fig. 9d) suggest a more complex subsurface structure, potentially influenced by lithological heterogeneity and fluid content. V_S is directly linked to the stiffness of geological materials and is widely used in geotechnical assessments of the near-surface[68,69]. The tomograms in Figures 8c and 9c delineate three distinct zones based on V_S values. The first zone, with a V_S range of 180 to 520 m/s, represents soft to stiff sediments, typically associated with unconsolidated materials such as sands, silts, and clays, and is indicative of sabkha deposits. These relatively low velocities suggest limited load-bearing capacity and increased susceptibility to deformation under stress, which has implications for infrastructure development in such areas[70]. Near the surface, sabkha layers are thin, with thicknesses ranging from 0.5 to 1.2 m (Fig. 3). These layers are interpreted as evaporitic facies, commonly composed of minerals such as gypsum and halite. Their presence further contributes to the mechanical weakness and variability of the uppermost sediments.

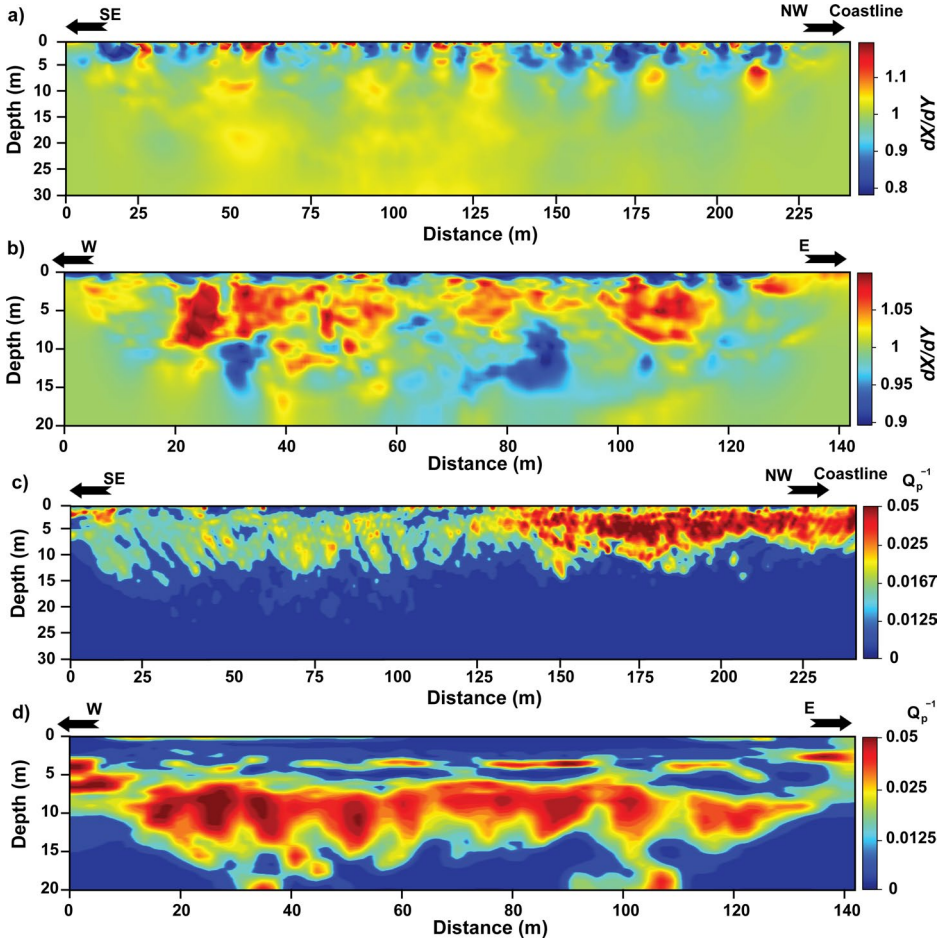

Fig. 10. 2D subsurface sections of derived seismic anisotropy (dX/dY) and attenuation ($Q_P{}^{-1}$). The ratio dX/dY was derived from the inversion of the V_P tomograms for the (**a**) CSAD and (**b**) SJUW sites, respectively. (**c**, **d**) Inverted $Q_P{}^{-1}$ profiles for CSAD (**c**) and SJUW (**d**). Significant attenuation and anisotropy magnitudes are concentrated in shallower zones, reflecting lithological variability and fluid-related effects.

The second zone, beginning at the boundary where V_S reaches approximately 460 m/s, marks a transition into denser sediments. This shift suggests increased compaction, potentially indicating a higher degree of consolidation or a distinct lithological formation. While this layer may offer improved stability compared to the overlying unconsolidated sediments, it does not possess the mec[7]hanical strength typically associated with geotechnical bedrock. The third zone, characterized by V_S values exceeding 760 m/s are interpreted as geotechnical bedrock. This layer exhibits significantly higher shear-wave velocities, indicating increased rigidity and reduced porosity, which suggests the presence of highly compacted sedimentary rock or lithified materials. These properties make it well-suited for geotechnical applications requiring stable, load-bearing substrates, such as heavy infrastructure development or seismic-resistant foundation design. Overall, the developing sabkha at SJUW exhibits relatively homogeneous subsurface conditions, likely due to minimal influence from sea-level fluctuations and slower continental processes. In contrast, the mature CSAD sabkha has been significantly shaped by the late Quaternary sea level changes[7,29], which involved multiple episodes of rapid transgression and regression. These dynamic processes have contributed to a more complex near-surface stratigraphy, reflected in its seismic properties and increased subsurface heterogeneity.

Sabkhas exhibit a distinctive hydrological regime, wherein groundwater recharge primarily occurs through the upward leakage of brines. This process is driven by the region's hot, arid climate and high evaporation rates. In the case of SJUW, recharge is sourced from continental brines and trapped paleo-seawater, whereas the CSAD sabkha is recharged predominantly by seawater flux. Dissolved solids in the sands underlying CSAD can exceed 300 g/L, while those in SJUW reach up to 180 g/L[2,7].

Previous studies by Eleslambouly, et al.[71] and Van Dam, et al.[72] using Electrical Resistivity Tomography (ERT) at CSAD revealed significant variations in the conductivity of subsurface sands. These variations are attributed to the dissolution of evaporites near the surface and the gravitational settling of heavy solutes into deeper aquifers. The V_P/V_S ratios derived from tomographic models (Figs. 8d and 9d) were used to delineate zones of varying fluid saturation. These results were further validated by comparing them with V_P/V_S ratios calculated from 1-D inverted V_S models and previously reported average V_P values per zone (Table 2). The consistency between these datasets supports the reliability of the interpretations. In CSAD, the shallowest layer, thinning toward

Parameter	First layer		Second layer		Third layer		Fourth Layer
	CSAD	SJUW	CSAD	SJUW	CSAD	SJUW	CSAD
Thickness (m)	0.95	1.1	2.8	4.4	10.3	7.5	16
V_P (m/s)	428	294	953	832	1917	2250	2534
V_S (m/s)	261	179	313	252	568	476	1032
Density (g/cc)	1.42	1.39	1.64	1.44	1.91	1.88	2.06
V_P/V_S	2.02	1.64	3.04	3.3	3.38	4.72	2.45
Poisson's modulus	0.2040	0.2055	0.4395	0.4495	0.4519	0.4766	0.4006
Description	Unconsolidated - dry sediments		Stiff - partially saturated		Dense - fully saturated		Hard - fully saturated layer

Table 2. Average computed parameters for each layer. The V_P obtained from Eleslambouly, et al.[24], While V_S obtained from the 1D MASW model in the present study.

the coastline is characterized by low V_P/V_S ratios, indicative of dry or poorly saturated sediments with fluid content below seismic sensitivity thresholds. Seasonal flooding in the northern parts may temporarily increase saturation, raising V_P; however, the unconsolidated nature of the sediments results in low stiffness and thus low V_P/V_S ratios (<1.5). The second zone, located at 1-5 m depth and extending to 6- 8 m, exhibits slightly higher ratios (not exceeding 2.4), suggesting partial saturation with residual gas trapped due to overburden pressure and capillary rise. The southeastern portion of this zone was not clearly resolved due to limited resolution at depth, although a V_P of 853 m/s was detected in this area[27]. A third zone beneath this sequence displays V_P/V_S ratios reaching up to 3.4, with lateral contrasts attributed to heterogeneous fluid properties. This interpretation aligns with findings by Eleslambouly, et al.[71] and Van Dam, et al.[72], who reported complex fluid mixing in these layers. The end of significant anisotropy contrast at approximately 13 m depth (Figs. 10a, Figs. 10b) further supports the transition to more homogeneous conditions at greater depths. Elevated V_P/V_S ratios near the coastline are likely due to high solid content in aquifer fluids, resulting from seasonal flooding and evaporite dissolution. At the base of the model, a dome-shaped boundary with V_P/V_S ratios near 2 are interpreted as a lithified, fully saturated rock layer. This zone exhibits reduced contrast, suggesting a more uniform seismic response beneath the sabkha sediments. The overall decrease in V_P/V_S ratio with depth is attributed to sediment strengthening through lithification and early diagenesis processes[73,74]. Attenuation data further support these interpretations. High ${Q_P}^{-1}$ values are observed in partially saturated zones, extending to an average depth of 14 m (Fig. 10c). These elevated attenuation magnitudes are likely due to fluid content and scattering effects caused by heterogeneities, particularly toward the seaside.

The SJUW profile exhibits stratigraphic zones similar to those observed in CSAD. A very thin, near-surface dry zone is characterized by a V_P/V_S ratio of approximately 2.3, followed by a partially saturated second zone at a depth of 1 m and extends to 5.5 m, with a higher V_P/V_S ratio. This second zone is vertically discontinuous in the eastern-middle portion of the section and transitions into a third, fully saturated zone with even higher V_P/V_S values (Fig. 9d). The partially saturated zone corresponds well with the borehole data reported by Eleslambouly, et al.[27], which indicates the water table at approximately 1 m depth. These findings are consistent with previously proposed hydrological conceptual models that describe artesian upwelling from deep aquifers[8,10,11,37,75–78]. It is assumed that overburden pressure drives upward leakage from these deep aquifers into shallower sediments, a process supported by the observed seismic data and models.

A general trend of decreasing V_P/V_S ratio with depth is evident, attributed to progressive sediment lithification and compaction. The partially saturated transition zone in SJUW is thicker than in CSAD, allowing it to be resolved by both conventional and high-resolution seismic methods, as demonstrated by Eleslambouly, et al.[27]. In contrast, the thinner transition zone in the mature CSAD sabkha was not resolved by conventional seismic techniques.

Two zones of high V_P gradients in Figure 9b correspond to the interfaces between partially and fully saturated layers. These transitions reflect the influence of pore fluid content, which stabilizes at greater depths. The attenuation coefficient section (Fig. 10d) shows elevated attenuation beginning in the partially saturated zone and extending to an average depth of 15 m, aligning with the V_P/V_S trend observed in the fully saturated zone. This correlation underscores the relationship between fluid saturation and seismic attenuation, particularly in the more homogeneous SJUW profile.

Anisotropy analysis reveals subsurface complexity, with each stratigraphic zone exhibiting distinct directional variations in V_P. Anomalies in the V_P/V_S ratio within the third zone corresponds to anisotropy contrasts, potentially linked to diagenetic processes or fluid heterogeneity. Overall, SJUW displays higher V_P/V_S ratios, reflecting the weaker mechanical properties of its sediments.

The identification of the partially saturated layer is consistent with borehole measurements and both conventional and high-resolution seismic data. In both sabkhas, this zone is attributed to weak overburden pressure and the presence of trapped air in pore spaces, with water rising due to capillary forces. Saturation increases gradually with depth, lacking a sharp interface; thus, head waves are not generated in the absence of a distinct boundary[24,79].

Conclusions

This study involved the acquisition of seismic profiles at the mature CSAD and the immature SJUW, using geophones spaced at 2-m intervals. The data were processed for seismic refraction and MASW to independently derive V_P and V_S tomograms. From these, the V_P/V_S ratio was computed, offering enhanced subsurface imaging capabilities in complex hydrological settings. Additionally, seismic anisotropy (dX/dY) and ${Q_P}^{-1}$ profiles were analyzed to interpret their relationship with sabkha features. The key findings of the study are:

- High-resolution V_S tomograms revealed the geotechnical bedrock at depths of approximately 15 m in CSAD and 12.5 m in SJUW. The seismic bedrock in CSAD was further mapped at an average depth of 65 m, whereas the bedrock in SJUW was not detected within the surveyed depth range, consistent with previous studies indicating deeper bedrock. CSAD exhibited a higher V_S (up to 380 m/s) in the upper meter due to the presence of a lithified hardground layer, whereas SJUW showed lower velocities (180-240 m/s), reflecting its unconsolidated sedimentary nature.
- V_P and V_S tomograms enabled distinguishing three hydrological zones in both sabkhas. The V_P/V_S ratio distinguished a very thin near-surface dry layer (1–5 m), an underlying partially saturated zone extending to ~6–8 m (thicker in SJUW), and a deeper fully saturated interval, validating existing geological conceptual models. In CSAD, seismic properties were strongly influenced by proximity to the sea, whereas SJUW showed a direct connection to deeper continental aquifers, with artesian flow pathways extending to shallow sediments.
- Variations in V_P in the deepest (fully statured) zone are consistent with mixed brine effects and correlate with higher attenuation. These are attributed to the mixing of continental and sabkha brines, which are hypersaline and not in equilibrium. This fluid mixing zone is responsible for significant seismic attenuation in both sabkhas. The fully saturated zone, characterized by high V_P/V_S ratios correspond to elevated attenuation magnitudes, particularly in CSAD, where seasonal flooding and evaporite dissolution likely contribute to the observed seismic responses.

Data availability

The CSAD and SJUW seismic datasets[80] were collected by Khalifa University and King Fahd University of Petroleum and Minerals (KFUPM), respectively, and are available at [https://doi.org/10.5281/zenodo.13937907]. Requests for access should be directed to the corresponding author, Ahmed Eleslambouly.

Received: 30 June 2025; Accepted: 19 November 2025
Published online: 27 November 2025

References

1. Warren, J. K. & Warren, J. K. Sabkhas, saline mudflats and pans. *Evaporites: Geolo. Compend.* https://doi.org/10.1007/978-3-319-13512-0_3 (2016).
2. Wood, W. W., Sanford, W. E. & Habshi, A. R. S. A. Source of solutes to the coastal sabkha of Abu Dhabi. *Geol. Soc. Am. Bull.* **114**, 259–268 https://doi.org/10.1130/0016-7606 (2002).
3. Al-Homidy, A. A., Dahim, M. H. & Abd El Aal, A. K. Improvement of geotechnical properties of sabkha soil utilizing cement kiln dust. *J. Rock Mech. Geotechn. Eng.* **9**, 749–760. https://doi.org/10.1016/j.jrmge.2016.11.012 (2017).
4. Al-Amoudi, O. S. B. & Abduljauwad, S. N. Compressibility and collapse characteristics of arid saline sabkha soils. *Eng. Geol.* **39**, 185–202 (1995).
5. Al-Amoudi, O. S. B., Abduljauwad, S. N. & El-Naggar, Z. R. Response of sabkha to laboratory tests: a case study. *Eng. Geol.* **33**, 111–125 (1992).
6. ArcGIS Pro v. 3.6 https://www.esri.com/en-us/arcgis/products/arcgis-pro/overview. (Environmental systems research institute, Redlands, CA, 2025).
7. Hussain, M., Al-Shaibani, A., Al-Ramadan, K. & Wood, W. W. Geochemistry and isotopic analysis of brines in the coastal sabkhas, Eastern region, Kingdom of Saudi Arabia. *J. Arid Environ.* **178**, 104142. https://doi.org/10.1016/j.jaridenv.2020.104142 (2020).
8. Patterson, R. & Kinsman, D. Hydrologic framework of a sabkha along Arabian Gulf. *AAPG Bull.* **65**, 1457–1475. https://doi.org/10.1306/03B5956C-16D1-11D7-8645000102C1865D (1981).
9. Al-Amoudi, O., El-Naggar, Z. & Siyed, I. The sabkha in the kingdom of Saudi Arabia and its engineering problems. *Al-Muhandis (Eng.)* **6**, 56–62 (1992).
10. Alsharhan, A. & Kendall, C. S. C. Interpretations of Holocene carbonate-evaporites of coastal and inland sabkhas of Abu Dhabi (United Arab Emirates) from Landsat satellite images and field survey. *Sabkha Ecosyst.: Volume VI: Asia/Pacific* https://doi.org/10.1007/978-3-030-04417-6_11 (2019).
11. Saeed, W., Shouakar-Stash, O., Unger, A., Wood, W. W. & Parker, B. Chemical evolution of an inland sabkha: a case study from Sabkha Matti, Saudi Arabia. *Hydrogeol. J.* https://doi.org/10.1007/s10040-021-02346-8 (2021).
12. Wood, W. W. An historical odyssey: the origin of solutes in the coastal sabkha of Abu Dhabi, United Arab Emirates. *Quat. Carbonate Evaporite Sediment. Facies Ancient Analog.: Tribut. Douglas James Shear.* https://doi.org/10.1002/9781444392326.ch11 (2010).
13. Kinsman, D. J. Modes of formation, sedimentary associations, and diagnostic features of shallow-water and supratidal evaporites. *AAPG Bull.* **53**, 830–840. https://doi.org/10.1306/5D25C801-16C1-11D7-8645000102C1865D (1969).
14. Hakami, B. A. & Seif, E.-S.S.A. Expansive potentiality of sabkha soils of Rabigh Lagoon, Saudi Arabia: a case study. *Arab. J. Geosci.* **12**, 1–14. https://doi.org/10.1007/s12517-019-4271-x (2019).
15. Sabtan, A. & Shehata, W. Problematic Sabkha–A potential source of fresh water. *Bull. Eng. Geol. Environ.* **61**, 153–159. https://doi.org/10.1007/s100640100133 (2002).
16. Akili, W. In *Proc. of the Geotechnical Problems in Saudi Arabia Symposium.* 775-793.
17. Ismael, N., Jeragh, A., Mollah, M. & Khaldi, O. In *Southeast Asian Geotechnical Conference 9,* 147-158.
18. Lokier, S. W. Coastal sabkha preservation in the Arabian Gulf. *Geoheritage* **5**, 11–22. https://doi.org/10.1007/s12371-012-0069-x (2013).
19. Gates, J. S., White, D., Stanley, W. & Ackermann, H. Availability of fresh and slightly saline ground water in the basins of westernmost Texas. Report No. 2331-1258, 62 (US Geological Survey Texas Department of Water Resources, 1980).
20. Al-Husseini, M. I., Glover, J. B. & Barley, B. J. Dispersion patterns of the ground roll in eastern Saudi Arabia. *Geophysics* **46**, 121–137. https://doi.org/10.1190/1.1441183 (1981).

21. Robinson, D. K. & Al-Husseini, M. I. Technique for reflection prospecting in the Rub'Al-Khali. *Geophysics* **47**, 1135–1152. https://doi.org/10.1190/1.1441377 (1982).
22. Adel, M., Deif, A., El-Hadidy, S., Sayed, S. M. & El Werr, A. Definition of soil characteristics and ground response at the northwestern part of the Gulf of Suez Egypt. *J. Geophys. Eng.* **5**, 420–437. https://doi.org/10.1088/1742-2132/5/4/006 (2008).
23. Al-Shuhail, A. & Al-Shaibani, A. M. Seismic investigation of two coastal sabkhas, eastern Saudi Arabia. *J. Seism. Explor.* **18**, 329–345 (2009).
24. Al-Shuhail, A. A. & Al-Shaibani, A. M. Characterization of Sabkha Jayb Uwayyid, eastern Saudi Arabia using seismic refraction profiling. *Arab. J. Geosci.* **6**, 845–855. https://doi.org/10.1007/s12517-011-0366-8 (2013).
25. El-Hussain, I. et al. Delineation of a paleo-channel utilizing integrated geophysical techniques at the port of duqm area, sultanate of oman. *J. Geophys. Eng.* **11**, 055005. https://doi.org/10.1088/1742-2132/11/5/055005 (2014).
26. Al-Heety, A. J., Hassouneh, M. & Abdullah, F. M. Application of MASW and ERT methods for geotechnical site characterization: a case study for roads construction and infrastructure assessment in Abu Dhabi. *UAE. J. Appl. Geophys.* **193**, 104408. https://doi.org/10.1016/j.jappgeo.2021.104408 (2021).
27. Eleslambouly, A. et al. Seismic properties of coastal and inland sabkhas: Implications for static corrections. *Earth Space Sci.* **12**, e2024EA003813. https://doi.org/10.1029/2024EA003813 (2025).
28. Paul, A. & Lokier, S. W. Holocene marine hardground formation in the Arabian Gulf: Shoreline stabilisation, sea level and early diagenesis in the coastal sabkha of Abu Dhabi. *Sediment. Geol.* **352**, 1–13. https://doi.org/10.1016/j.sedgeo.2017.02.005 (2017).
29. Kirkham, A. & Evans, G. Carbonate sedimentation around Jebel Dhanna: models for parts of the buried Holocene sabkha sequences elsewhere along the Abu Dhabi coastline. *Carbonates and Evaporites* **35**, 1-11 s13146-020-00561-0 (2020).
30. Hadley, G. D., Brouwers, M. E. & Bown, M. T. In *Quaternary Deserts and Climatic Change* 123-139 (CRC Press, 2020).
31. Farrant, A. R. et al. Developing a framework of quaternary dune accumulation in the northern Rub'al-Khali Arabia. *Quat. Int.* **382**, 132–144. https://doi.org/10.1016/j.quaint.2015.02.022 (2015).
32. Rankey, E. C. & Berkeley, A. Holocene carbonate tidal flats. *Principles of Tidal Sedimentology*, 507-535 https://doi.org/10.1007/978-94-007-0123-6_19 (2012).
33. Kirkham, A. & Evans, G. Aspects of the Abu Dhabi Sabkha. *Sabkha Ecosystems: Volume VI: Asia/Pacific* 15-40 https://doi.org/10.1007/978-3-030-04417-6_3 (2019).
34. Nairn, A. & Alsharhan, A. *Sedimentary basins and petroleum geology of the Middle East* (Elsevier, 1997).
35. Arman, H., Abdelghany, O., Saima, M. A., Aldahan, A. & Paramban, S. Petrographical and geoengineering characteristics of evaporitic rocks (Abu Dhabi city vicinity, United Arab Emirates). *Arab. J. Geosci.* **14**, 1–7. https://doi.org/10.1007/s12517-021-08318-2 (2021).
36. Abdelghany, O., Abu Saima, M., Arman, H. & Fowler, A. In *International Conference on Engineering Geophysics, Al Ain, United Arab Emirates, 15-18 November* 164-167 (Society of Exploration Geophysicists). (2015)
37. Alsaaran, N. A. Origin and geochemical reaction paths of sabkha brines: Sabkha Jayb Uwayyid, eastern Saudi Arabia. *Arab. J. Geosci.* **1**, 63–74. https://doi.org/10.1007/s12517-008-0005-1 (2008).
38. Doebrich, J. L. & Smith, C. L. Drilling in sabkhahs of the Dhahran area, Kingdom of Saudi Arabia. Report No. 80-323, (1979).
39. Dimock, W. Sabkhah Jab Awaiyid halite deposit. *Open File Report, Saudi Arabian Directorate General of Mineral Resources Saudi Arabia* **441** (1955).
40. Smith, C. L. Proposed method of hydrogeochemical exploration for salt deposits using ClBr ratios, Eastern Province Kingdom Saudi Arabia. *Appl. Geochem.* **6**, 249–255. https://doi.org/10.1016/0883-2927(91)90002-7 (1991).
41. Al-Shaibani, A. Economic potential of brines of Sabkha jayb uwayyid, eastern Saudi Arabia. *Arab. J. Geosci.* **6**, 2607–2618. https://doi.org/10.1007/s12517-012-0521-x (2013).
42. Liu, Q. & Gu, Y. Seismic imaging: from classical to adjoint tomography. *Tectonophysics* **566**, 31–66. https://doi.org/10.1016/j.tecto.2012.07.006 (2012).
43. Azwin, I., Saad, R. & Nordiana, M. Applying the seismic refraction tomography for site characterization. *APCBEE procedia* **5**, 227-231 https://doi.org/10.1016/j.apcbee.2013.05.039 (2013).
44. Lines, L. & Treitel, S. A review of least-squares inversion and its application to geophysical problems. *Geophys. Prospect.* **32**, 159–186. https://doi.org/10.1111/j.1365-2478.1984.tb00726.x (1984).
45. Abraham, O., Slimane, K. B. & Cote, P. Factoring anisotropy into iterative geometric reconstruction algorithms for seismic tomography. *Int. J. Rock Mech. Mining Sci.* **35**, 31–41. https://doi.org/10.1016/S0148-9062(97)00002-8 (1998).
46. Cardarelli, E. Ray tracing applied to travel time seismic tomography (theory and examples). *Bollettino di geofisica Teorica ed Applicata* **44**, 281–305 (2003).
47. Aki, K. & Richards, P. G. Quantative seismology: theory and methods. In *Quantative Seismology: Theory and Methods. by K. Aki and PG Richards* https://doi.org/10.1002/gj.3350160110 (Freeman, San Francisco, 1980).
48. Taipodia, J. & Dey, A. In *National Workshop Engineering Geophysics for Civil Engineering and Geo-hazards (EGCEG).* (Roorkee CBRI).
49. Hayashi, K. & Suzuki, H. CMP cross-correlation analysis of multi-channel surface-wave data. *Explor. Geophys.* **35**, 7–13. https://doi.org/10.1071/EG04007 (2004).
50. Xia, J. et al. High-frequency rayleigh-wave method. *J. Earth Sci.* **20**, 563–579. https://doi.org/10.1007/s12583-009-0047-7 (2009).
51. Hubbard, S. S. & Rubin, Y. In *The Handbook of Groundwater Engineering* 877-914 (CRC Press, 2016).
52. Grelle, G. & Guadagno, F. M. Seismic refraction methodology for groundwater level determination:"Water seismic index". *J. Appl. Geophys.* **68**, 301–320. https://doi.org/10.1016/j.jappgeo.2009.02.001 (2009).
53. Mavko, G., Mukerji, T. & Dvorkin, J. *The rock physics handbook* (Cambridge University Press, 2020).
54. Biot, M. A. Theory of elastic waves in a fluid-saturated porous solid. 1. Low frequency range. *J. Acoust. Soc. Am.* **28**, 168–178. https://doi.org/10.1121/1.1908239 (1956).
55. Davis, J. L. *Wave propagation in solids and fluids* (Springer Science & Business Media, 2012).
56. Conte, E., Cosentini, R. M. & Troncone, A. Geotechnical parameters from VP and VS measurements in unsaturated soils. *Soils Found.* **49**, 689–698. https://doi.org/10.3208/sandf.49.689 (2009).
57. Pasquet, S. et al. 2D characterization of near-surface VP/VS: Surface-wave dispersion inversion versus refraction tomography. *Near Surface Geophys.* **13**, 315–332. https://doi.org/10.3997/1873-0604.2015028 (2015).
58. Singh, N. et al. In *International Conference on Advances in Structural Mechanics and Applications*. 412-425 (Springer).
59. Vantassel, J. P. & Cox, B. R. SWprocess: a workflow for developing robust estimates of surface wave dispersion uncertainty. *J. Seismol.* **26**, 731–756. https://doi.org/10.1007/s10950-021-10035-y (2022).
60. Foti, S. et al. Guidelines for the good practice of surface wave analysis: a product of the InterPACIFIC project. *Bullet. Earthq. Eng.* **16**, 2367–2420. https://doi.org/10.1007/s10518-017-0206-7 (2018).
61. Mohamed, A. M., El Ata, A. A., Azim, F. A. & Taha, M. Site-specific shear wave velocity investigation for geotechnical engineering applications using seismic refraction and 2D multi-channel analysis of surface waves. *NRIAG J. Astron. Geophys.* **2**, 88–101. https://doi.org/10.1016/j.nrjag.2013.06.012 (2013).
62. Abdelbaky, M., Kassab, W. & El-Anbaawy, M. Geotechnical integrated approach to evaluate the karst hazard potentiality in the qatar coastal eocene carbonate bedrocks. *Bulletin of Faculty of Science, Zagazig University* 131-153 (2022).
63. Alarifi, S. S. Surface and subsurface sinkholes and karstic cavities in the uppermost jurassic-lower cretaceous sulaiy formation in an Narjis District, Riyadh, Central Saudi Arabia: field and geophysical investigation. *J. Appl. Geophys.* **233**, 105612. https://doi.org/10.1016/j.jappgeo.2024.105612 (2025).

64. Nawaz, B. A., Spyropoulos, E. & Al-Saafin, A. K. Risk assessment for karst hazards at a facility in Saudi Arabia—a case study. *J. Geosci. Environ. Prot.* **8**, 277–312. https://doi.org/10.4236/gep.2020.85018 (2020).
65. Albesher, Z. I., Alotaibi, A. & Aljabbab, A. Identifying subsurface weak zones in Riyadh of surface wave technique. *Journal of King Saud*https://doi.org/10.25259/JKSUS_456_2025 (2025).
66. Evans, G., Kendall, C. S. C. & Skipwith, P. Origin of the coastal flats, the sabkha, of the Trucial Coast. *Persian Gulf. Nat.* **202**, 759–761. https://doi.org/10.1038/202759a0 (1964).
67. Lokier, S. & Steuber, T. Quantification of carbonate-ramp sedimentation and progradation rates for the late Holocene Abu Dhabi shoreline. *J. Sediment. Res.* **78**, 423–431. https://doi.org/10.2110/jsr.2008.049 (2008).
68. Park, C. MASW for geotechnical site investigation. *Lead. Edge* **32**, 656–662. https://doi.org/10.1190/tle32060656.1 (2013).
69. Ashraf, M. M., Kumar, N., Yusoh, R., Hazreek, Z. & Aziman, M. In *Journal of Physics: Conference Series.* 012108 (IOP Publishing).
70. Sundararajan, N. et al. Shear wave velocity characteristics in parts of Muscat, Sultanate of Oman—a measure of earthquake hazard assessment. *J. Geol. Soc. India* **93**, 515–522. https://doi.org/10.1007/s12594-019-1212-y (2019).
71. Eleslambouly, A. et al. In *6th Asia Pacific Meeting on Near Surface Geoscience and Engineering.* 1-5 (European Association of Geoscientists & Engineers).
72. Van Dam, R. L., Simmons, C. T., Hyndman, D. W. & Wood, W. W. Natural free convection in porous medi first field documentation in groundwater. *Geophys. Res. Lett.* https://doi.org/10.1029/2008GL036906 (2009).
73. Scholle, P. A. & Halley, R. B. Burial diagenesis: out of sight, out of mind!. *Carbonate Sedimentol. Petrol.* **4**, 135–160. https://doi.org/10.1029/SC004p0135 (1989).
74. Krystinik, L. In Rocky Mountain Section (SEPM).
75. Yechieli, Y. & Wood, W. W. Hydrogeologic processes in saline systems: playas, sabkhas, and saline lakes. *Earth-Sci. Rev.* **58**, 343–365. https://doi.org/10.1016/S0012-8252(02)00067-3 (2002).
76. Johnson, D. H., Kamal, M. R., Pierson, G. O. & Ramsay, J. B. Sabkhas of eastern Saudi Arabia. *Quat. Period Saudi Arabia* **1**, 84–93. https://doi.org/10.1007/978-3-7091-8494-3 (1978).
77. Al-Hurban, A. & Gharib, I. Geomorphological and sedimentological characteristics of coastal and inland sabkhas, Southern Kuwait. *J. Arid Environ.* **58**, 59–85. https://doi.org/10.1016/S0140-1963(03)00128-9 (2004).
78. McKay, C. P. et al. An unusual inverted saline microbial mat community in an interdune sabkha in the Rub'al Khali (the Empty Quarter) United Arab Emirates. *PloS one* **11**, e0150342. https://doi.org/10.1371/journal.pone.0150342 (2016).
79. Sjogren, B. *Shallow refraction seismics*. 5-10 (Springer Science & Business Media, 2013).
80. Eleslambouly, A. CSAD and SJUW Seismic Data [Dataset]. Zenodo. https://doi.org/10.5281/zenodo.13937908 (2024).

Acknowledgments

The authors gratefully acknowledge the support provided by Khalifa University and King Fahd University of Petroleum and Minerals for facilitating the data acquisition and fieldwork essential to this study.

Author contributions

A.E., A.A.-S., A.E.H., and M.Y.A. conceptualized the study. Methodology was developed by A.E., M.Y.A., and F.B. Software implementation and field investigations were carried out by A.E. M.Y.A, and F.B. Formal analysis and visualization were performed by A.E. and F.B. Data curation and resource coordination were led by A.E., M.Y.A., A.A.-S., and A.E.H. Validation of results was conducted by J.M. and S.M.H. The original manuscript draft was written by A.E. Review and editing were contributed by A.E., M.Y.A., A.A.-S., A.E.H., J.M., and S.M.H. Supervision was provided by M.Y.A., F.B., A.E.H., and A.A.-S. Funding acquisition was the responsibility of M.Y.A.

Funding

This research was supported by Khalifa University (Grant No. 8474000730).

Declarations

Competing interests

The authors declare no competing interests.

Additional information

Supplementary Information The online version contains supplementary material available at https://doi.org/10.1038/s41598-025-29863-w.

Correspondence and requests for materials should be addressed to A.E.

Reprints and permissions information is available at www.nature.com/reprints.

Publisher's note Springer Nature remains neutral with regard to jurisdictional claims in published maps and institutional affiliations.